UXO DETECTION AT JEFFERSON PROVING GROUND USING GROUND-PENETRATING RADAR

Steven A. Arcone (tel 603 646 4368, fax 603 646 4644, sarcone@crrel.usace.army.mil)
Allan J. Delaney (tel 603 646 4252, fax 603 646 4644,
delaney@crrel.usace.army.mil)
Paul V. Sellmann (tel 603 646 4347, fax 603 646 4820)
Kevin O'Neill (tel 603 646 4312, fax 603 646 4820,
koneill@crrel.usace.army.mil)
U. S. Army Cold Regions Research and Engineering Laboratory
72 Lyme Road
Hanover, NH 03755

UXO FORUM '98
Anaheim, California
May 5–7, 1998

ABSTRACT

We have used ground-penetrating radar (GPR) to detect UXO and non-ordnance on the 40-acre site (lot 54) of Jefferson Proving Ground, Indiana. The UXO are buried within about 1 m deep in a clayey silt for which the soil water content ranged from moist near the surface to near saturation at about 1 m. We used a 16-bit radar to profile along previously established lines, and transects over artificial targets we emplaced. We recorded data at 48–64 traces/s with minimal towing speeds during both dry and rainy weather. Target responses at both 300 (time range of 50 ns) and 600 MHz (30 ns) ranged from discrete diffractions to short reflection segments. The loss of the soil greatly attenuated diffraction hyperbolas. Theoretical analyses of these hyperbolas give an average soil dielectric constant of 10 at both 300 and 600 MHz. The phase polarity of many of the reflected and diffracted wavelets indicate targets with wave impedances higher than that of the soil. We therefore assume these targets to be metallic and the responses of some, whose locations correlate with the position of UXO on burial maps, are shown in detail. Theoretical modeling of wavelet propagation for this soil confirms the high rate of attenuation (47–66 dB/m round trip), the maintenance of waveform, a shift in wavelet local frequency, and response to a typical UXO. We conclude that GPR is effective for finding targets in this type of soil to no more than 2 m depth. We recommend that future surveys utilize high trace acquisition rates to capture the full target responses and a prowed, heavy dielectric antenna sled to improve antenna-to-ground coupling and deflect surface obstacles such as vegetation.

INTRODUCTION

The remote detection of unexploded ordnance (UXO) has generally relied on the electromagnetic induction (EMI) and ground-penetrating radar (GPR) methods. EMI, the most common method, finds targets that contrast strongly in electrical conductivity with their host soil by detecting 10- to 40-kHz magnetic fields induced from the target. EMI systems are mobile and do not require ground contact, and their performance is not degraded by minor variations in topography. However, they have little ability to detect nonmetallic targets. GPR, which generally operates between about 50 and 1000 MHz, is sensitive to contrasts in both conductivity and dielectric permittivity. Thus GPR can detect plastic, glass, concrete or wood when their permittivity contrasts with that of a moist soil. In addition, GPR shows the continuity of soil horizons and thus can detect burials of foreign targets by the disturbance of those horizons. GPR performance requires good antenna–ground contact and a complex soil permittivity and conductivity that does not rapidly attenuate radiowave energy. The 50- to 300-MHz range usually provides optimum penetration for a given soil conductivity and permittivity. In this report we discuss GPR results from a site within the Jefferson Proving Ground (JPG), where ordnance is buried within a highly attenuating soil and for which reports of GPR performance (NAVEOD, 1997) are negative.

Our objective was to assess the ability of GPR to detect UXO-type targets at JPG. In particular, we were interested in the effect of the soil electrical properties upon the GPR survey parameters of frequency, towing speed, and data aquisition rate. We surveyed a site where the types, locations, depths, and approximate orientations of both ordnance (metallic) and non-ordnance (metallic and non-metallic) are documented. We used supplied location maps to identify the probable nature of targets detected. The specified depths are rarely stated to exceed one meter. We used a commercially available GPR system and towed 100-, 300- and 600-MHz (mid-band values) frequency antennas along established lines. The higher two frequencies provide high resolution of subsurface objects and are within military specification for ordnance detection, and the antennas are small and mobile. We used the signal characteristics obtained from ordnance, non-ordnance, and objects we emplaced to determine soil permittivity and diffraction waveforms.

SITE DESCRIPTION

JPG (**Fig. 1**) is located in southern Indiana. Our investigations were performed within lot 54, known as the 40-acre site (**Fig. 1**). The vegetation at this site is predominantly sedge and grass with a few trees. The area has a nearly level to gently sloping topography with small gullies providing less than a few meters of relief. The site has been specially prepared with approximately 246 unfused, buried ordnance and 234 non-ordnance targets buried within 1 m of the surface. The ordnance includes small, hand-held munitions, 2-ft- (0.6-m) long projectiles and 5-ft- (1.6-m) long bombs. Strong radio background noise was present at this site.

We conducted our surveys on October 23–25, 1997. The weather was clear on 23 October, and then light rain fell late on the 24 and all day on 25 October. All of our profile transects were freshly mowed, but clumps of woody vegetation and tractor ruts made for uneven antenna towing and short periods of poor antenna–ground contact.

SOILS

The soils in this area formed in a thin surface layer of wind-blown silt (loess) and underlying glacial drift (Nickell, 1985). Some residual soils may reside near the limestone bedrock interface where small rock fragments occur. The bedrock ranges from about 1.5 to 7.6 m deep. The soils are part of either the Cobbsfork-Avonburg (CA) or Cincinnati-Rossmoyne-Hickory (CRH) soil map

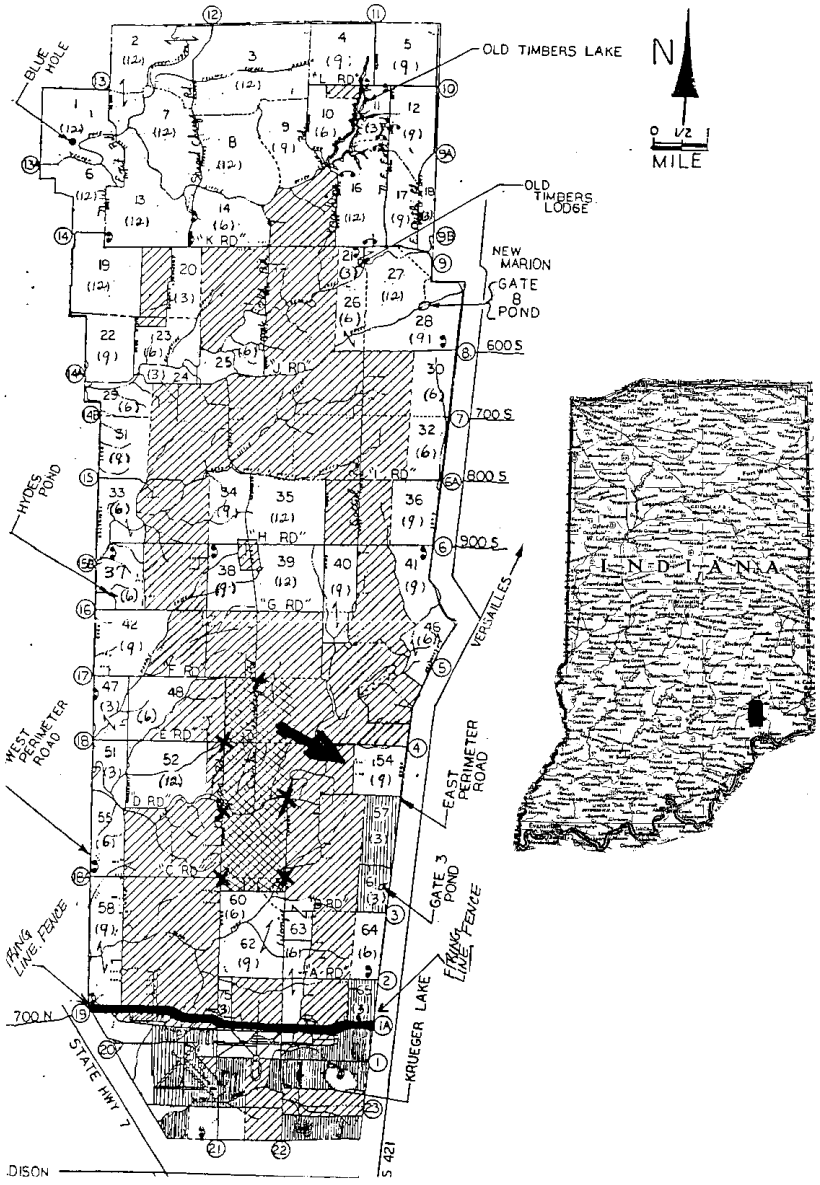

Figure 1. Location of the 40-acre site at Jefferson Proving Ground.

units. The CA soils are found on level to gently sloping surfaces, are generally poorly drained, and have a seasonally high water table. They can also have a pan layer, which can create a perched water table at a depth of 0.3–1 m for a significant part of the year. The CRH soils are found on level to steep surfaces and are classed as well drained to moderately well drained. They may also have a pan layer of low permeability and perched water tables at depths of 0.5–1 m during the winter and spring. In general, both soil units have a 15- to 20-cm surface soil consisting of silt loam varying from dark brown to gray brown. The permeability tends to decrease with depth due to an increase in clay content in the pan layers.

X-ray diffraction studies performed by the U.S. Army Waterways Experiment Station in Vicksburg, MS show the soil mineralogy to be primarily quartz and plagioclase feldspar with clay minerals generally absent or in minor amounts. This is consistent with other studies of loess in the southern U. S. (Rodbell et al., 1997), which show a predominant amount of quartz, and also with studies of loess in interior Alaska (Pewe, 1955).

DIELECTRIC THEORY

We present the theory of radiowave propagation in soils in this section in order to provide a basis for modeling the GPR propagation at JPG later. The discussion pertains to engineering-grade silt- and clay-size soils, but of little clay mineralogy so that it applies to the soils at JPG. The radar detectability of a subsurface target strongly depends on the radiowave speed, v, and attenuation rate, β, of the burial soil. The speed determines the shape of the antenna beamwidth. β determines how deep the radiowaves will penetrate and return to the surface with enough strength to be detected. These quantities are related to the relative complex permittivity of soil, ε_s^*, such that

$$v = c/\text{Real}\,(\varepsilon_s^{*1/2}) \tag{1}$$

and

$$\beta(\text{dB/m}) = 20\log\,[\exp(-i\omega/c(\text{Imag}(\varepsilon_s^{*1/2})))] \tag{2}$$

where $i = (-1)^{1/2}$, ω is frequency in radians/s, and $c = 3 \times 10^8$ m/s is the wavespeed in free space. The quantity ε_s^* is determined by the Debye relaxation permittivity (Debye, 1929), ε_{rel}, and a contribution from the very-low-frequency soil conductivity, σ(Siemens/m, or S/m), such that

$$\varepsilon_s^* = \varepsilon_{rel} - i\sigma/\omega\varepsilon_0 \tag{3}$$

where

$$\varepsilon_{rel} = \varepsilon_{oo} + (\varepsilon_{st} - \varepsilon_{oo})/(1 + i\, f/f_{rel}) \tag{4}$$

ε_0 is the dielectric permittivity of free space (a constant), ε_{st} is the low-frequency, "static" value of the relative soil permittivity, ε_{oo} is the very-high-frequency value, $f = 2\pi\omega$ is the wave frequency in Hertz (Hz), or frequency component for a radar wavelet, and f_{rel} is the soil relaxation frequency. The quantity ε_{rel} determines the dipole moment density induced in a material by a passing wave. The quantity f_{rel} is a characteristic frequency above which the induced dipoles no longer stay in phase with the incident radiowave. These dipoles then generate interference, which effectively slows and attenuates the incident radiation. This process is dispersive, which means that different frequencies within the incident wavelets propagate at different speeds and attenuation rates (Brillouin, 1960; Stratton, 1941; and Feynman et al., 1964).

Values of ε_{st} are directly related to the water content for non-mineralogic clays and silts (Topp et al., 1980) and generally equal ε_s^* for $f < 600$ MHz. Above about 600 MHz laboratory investigations (Hoekstra and Doyle, 1971; Hoekstra and Delaney, 1974) show that the adsorbed water on the particle surfaces of the silt-clay fraction (Tice et al., 1982) strongly influences the dielectric properties. The adsorption process lowers both the high dielectric constant (81) of the normally free water and also the free water relaxation frequency (22 GHz) to about 1–3 GHz. Values of ε_{oo} are generally related to the dry soil density, range from about 2.5–3.5, and equal ε_s^* at frequencies above about 100,000 MHz. For soils of JPG and the radar frequencies used, σ was large enough to also influence attenuation because it determines how much of the radiowave energy will be converted into conduction currents.

The resulting values of ε_s^* for silty and clay-rich soils at frequencies above about 100 MHz provide high values of β and wave speeds lower than would be expected for sandy soils with the same volumetric water content. The β values (a quantitative discussion is given later) increase as f

approaches, and then exceeds, f_{rel}, and are orders of magnitude greater than attenuation rates caused by the geometric spreading of the radiation energy. At frequencies below about 1000 MHz, the real part, $\varepsilon' = \varepsilon_{st}$, often referred to as the dielectric constant, determines the wave speed v through the relation

$$v = c/\varepsilon'^{1/2} \tag{5}$$

for a variety of frozen and unfrozen silts and (non-mineralogic) clays (Hoekstra and Delaney, 1974; Topp et al., 1980; Delaney and Arcone, 1984).

EQUIPMENT AND METHODS

Radar system

We used the GSSI (Geophysical Survey Systems, Inc.) SIR system model 2 and models 3207 (100 MHz), 5103 (300 MHz), and 101C (600 MHz) antenna transducers. We used the control unit to set the time range (in nanoseconds, ns) for the echo traces, the data aquisition rate (48 or 64 traces/s), the sampling density (512 samples per trace), trace sample density (16-bit), and time variable gain (TVG) for the traces. We calibrated our settings with the antennas set over targets that we emplaced. The resulting reflections required a large amount of gain (up to 65 dB) at time ranges of only 50 (300 MHz) and 30 ns (600 MHz). The short time ranges were sufficient to capture target responses throughout the site but were also necessary to limit background radiowave interference, which beat with the radar returns at the high-gain time ranges. The high gain had the negative effect of amplifying small antenna impedance mismatches and low-amplitude clutter (unwanted events), which probably originated from radiation that leaked onto the antenna housing and cables. These events usually arrive at constant time delay and their interference can be alleviated with a horizontal "background removal" filter. However, in our case where short time ranges were used, electronic jitter and erratic movement of the antenna may have caused these events to arrive at variable amplitude and so their interference was not consistently reduced by filtering.

All antennas were resistively loaded dipoles. The smaller, 300- and 600-MHz antennas are shielded with semi-cylindrical housings to alleviate above-surface clutter. These frequencies are "local" (also known as "instantaneous") values, which correspond with the dominant periods and lie approximately at the center of the received wavelet spectrum. They are considerably below the manufacturer's specifications for these antennas (400 and 900 MHz, respectively), which generally apply to operation in air or on the ground with lower values of dielectric permittivity and loss than encountered here. Their transmitters do not exceed 8 W (peak power) in order to protect the nearby receiver. 100-MHz data were also acquired but are not discussed because the direct coupling between these antennas, which lasts approximately 30–50 ns, obliterated any near-surface returns. The antenna directivity becomes increasingly confined beneath the antenna as ε' increases (Arcone, 1995). The typical shape of a transmitted GPR wavelet for either the 300- or 600-MHz antenna system is shown in **Figure 2.** The phase polarity sequence of the half-cycles defines the wavelet phase (Arcone, 1995).

Field profiling

We profiled along established transects and entered electronic event markers on the profiles at previously established, 100-ft (30-m) distance marks. The transects generally deviated from a straight line by 1–2 m but sometimes as much as 5 m to avoid isolated bushes, trees and severe ruts. Consequently we cannot reconstruct our exact position along the lines, and errors of as much as 20 ft (6 m) may occur in our interpretation of distance between markers. We dragged all our antennas by

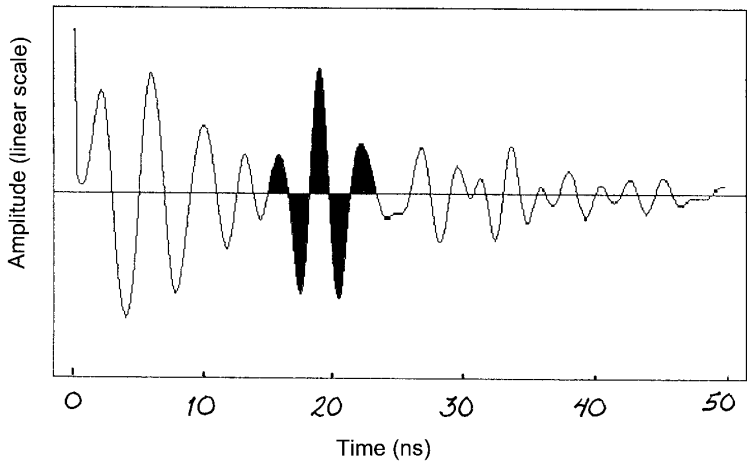

Figure 2. Typical form of a radiated GPR wavelet (darkened area). The frequency characterization of the wavelet refers to the inverse of the dominant wavelet period, in this case about 300 MHz.

vehicle at less than 1 m/s for long distances and by hand for the small surveys over emplaced targets. All antennas were polarized perpendicular to the transect direction. We determined that vehicle reflections were not in the data by comparing profiles recorded with and without the vehicle. We placed the smaller antennas in a fiberglass box to alleviate erratic antenna-to-ground coupling. However, the uneven towing speed over the rough ground also degraded the appearance of the profiles.

Post-processing and display of data

We first band-pass-filtered (very wide settings; e.g., 50–600 MHz for the Model 5103 antenna) the recorded data to alleviate high-frequency electronic noise and low-frequency, above-surface clutter. We normalized the number of data traces between event markers over the targets we emplaced to compensate for changes in dragging speed. We did not normalize the longer profiles with the 100-ft (30-m) marker spacing because vehicle speed varied between any two markers.

We use both linear and nonlinear gray-scale formats to indicate signal strength. We used an amplitude format to display the profiles for the targets we buried. In this format, positive phase is indicated by lighter tones and negative phase by darker tones. We used an intensity format to display the profiles of the permanent targets at JPG. In this format, which is insensitive to phase, strength is indicated by the intensity of darker tones.

Profile interpretation

The main objectives of the profile analysis are to determine if ordnance targets had been detected and the range of ε' values for the site soil. The permittivity analysis used the diffractions caused by radar scattering from targets. In this method we matched the hyperbolic shape of the diffractions with theoretical hyperbolas for a given value of ε' (Jezek et al., 1979; Clarke and Bentley, 1994; Arcone et al., 1998). The main disadvantages of this approach are (1) the hyperbolas can actually be responses to linear soil inclusions, in which case the hyperbolas are distorted reflections that result when the transect obliquely intersects the inclusion direction (Jezek et al., 1980) and are thus artificially wide; and (2) an erratic towing speed, which would distort the hyperbolic image. Item (1) was not considered important because of the depositional process of the soil (glacial drift and loess) and because of probable historical tilling. Number (2) is a concern and for this reason a statistical study is presented.

Target detection depends on the presence of either or both diffractions and reflections and also on their phase polarity. Both the strength and phase polarity of a reflected or diffracted event depend on the reflectivity of a target, which is determined by its Fresnel reflection coefficient, *R*, such that

$$R = (\varepsilon_s{}^{*1/2} - \varepsilon_t^{1/2})/(\varepsilon_s{}^{*1/2} + \varepsilon_t^{1/2}) \quad (6)$$

where ε_t is the complex permittivity for the target medium (Wait, 1970). Although this formula applies to plane wave incidence upon large flat reflectors, we invoke its use because of the small *in situ* wavelengths (30 cm at 300 MHz) relative to the larger sizes of some of the targets known to be buried at JPG and because it predicts the correct phase polarity. For a metal target, assumed to be ordnance, ε_t is orders of magnitude higher than $\varepsilon_s{}^*$ and produces a wavelet with a phase structure opposite to that produced when ε_t is lower than $\varepsilon_s{}^*$.

It is unlikely that any geologic or organic inhomogeneity in the JPG soil we profiled had a higher ε_t than that of the soil itself. Consistent horizons are virtually absent in our data, which means that electrically important changes, such as in moisture content, were gradational. In addition, ε' of limestone is generally between 8 and 10 (Parkhomenko, 1967), which is near that of the soil and precluded strong bedrock reflections.

RESULTS AND DISCUSSION

Control studies

Our objectives for the control studies were to obtain profile responses and scattered waveforms for buried metal reflectors, as well as soil moisture and conductivity profiles. We conducted these studies either outside or along the perimeter of the 40-acre site (**Fig. 3**). We buried two, 9-inch- (23-cm) diameter metal disks at depths of 11 (28 cm) and 23 (58 cm) inches. The removed soil was highly compact and did not appear to have excess moisture. Therefore, we think that no significant soil drying took place between removal and reburial. The 300- and 600-MHz diffractions from the deeper target (**Fig. 4**) (the response to the more shallow target is not sufficiently separated from the direct coupling between antennas to facilitate analysis) best fit theoretical diffraction hyperbolas for $\varepsilon' = 9.3$ and 8.6 at 300 and 600 MHz, respectively. The values of ε', which we computed from the wavelet round-trip travel time when the antennas were over the center of the targets, are 9.5 and 8.7, respectively. In accordance with the measurements, dielectric dispersion theory (**eq. 4**, and discussed below) predicts that the 600-MHz value should be slightly less than the 300-MHz value.

The accompanying traces in **Figure 4**, whose positions within the profiles are indicated by arrows, show the forms of the scattered wavelets within the diffractions. The wavelets have a negative-positive-negative sequence to the phase polarity of the dominant half-cycles. This sequence is typical for the relative polarity wiring of GSSI antennas and is characteristic of targets whose wave impedance (**eq. 6**) is higher than that of the surrounding media. Targets characterized by an ε' value less than that of the soil matrix would produce a similar wavelet but with opposite phase polarity of the individual half-cycles. The local frequency is indicated for the wavelets.

The amplitude along the 600-MHz hyperbolic asymptotes in **Figure 4** rapidly fades with distance from the target. This indicates a very high soil attenuation rate per meter; the change in antenna directivity with angle to the target (discussed later) is an insignificant loss factor. Commercial GPR systems at these frequencies commonly have a performance figure of about 100–120 dB and a dynamic range (the amplitude range visible in any particular trace) of about 60–70 dB. This latter range is consistent with the gain we added before recording and with soil attenuation rates discussed later.

The volumetric water content profiles of soil core samples (obtained before rain occurred) show values from about 15% at the surface to as high as 40% at 30–180 cm deep (**Fig. 5**). The water

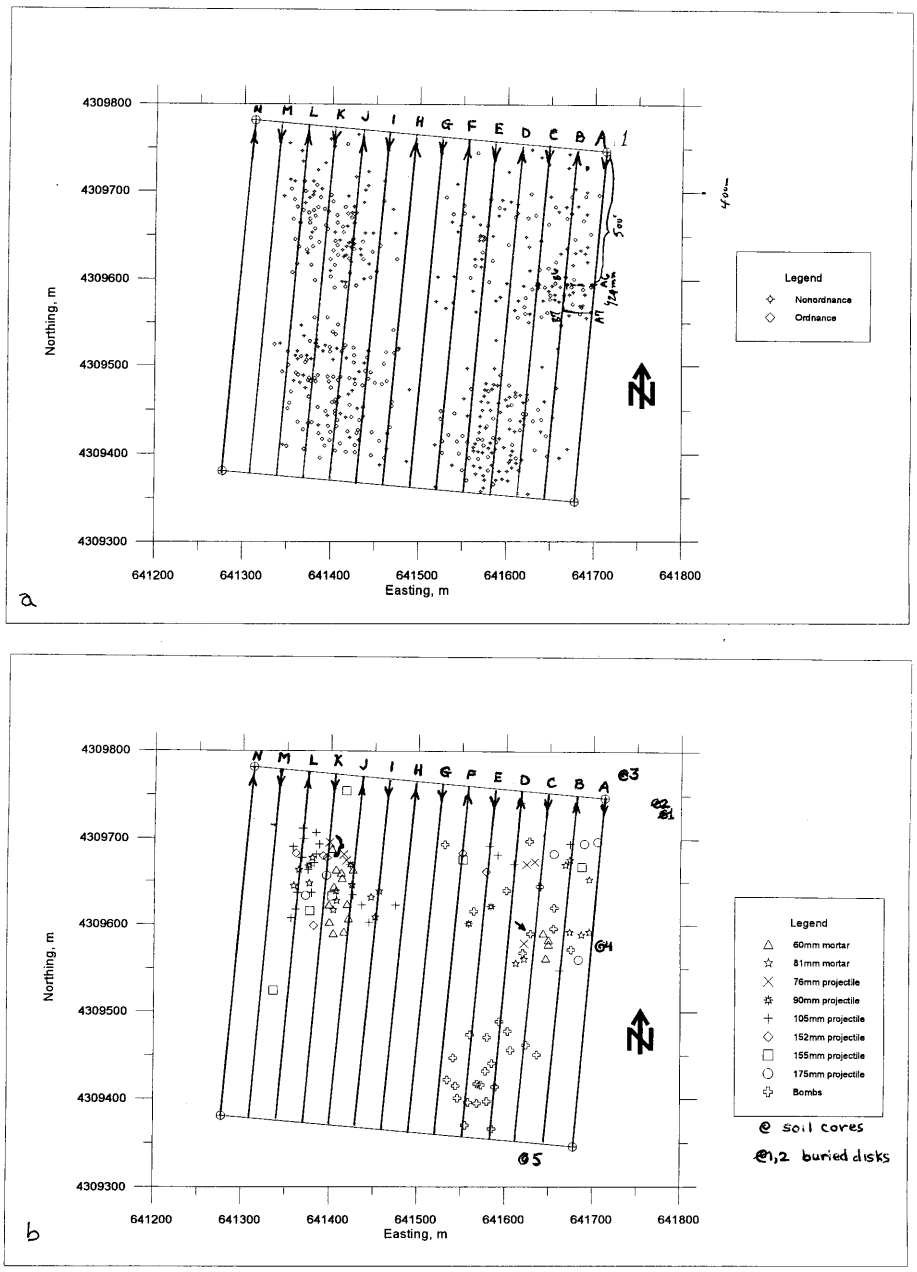

Figure 3. Ordnance and non-ordnance (a) and ordnance type (b) distributions at the 40-acre site with radar profile transects superimposed. Line arrows indicate the profile directions. In Figure 3b, the heavy arrow along line C marks a bomb (open cross symbol), and a bracket along line K indicate targets whose responses are discussed later. Also shown are the locations (spiral symbols) of the targets we buried and the soil cores we extracted for moisture profiles.

contents within the profile of the core obtained about 24 hours after steady rain had begun ranged from 23 to 45%, the latter of which is at about saturation for this type of soil. The core obtained above the 58-cm-deep target showed a moisture content that varied from 15% at 15 cm deep to 24% at 50–70 cm deep. According to Topp et al. (1980), these water contents correspond with ε' values ranging from about 7 (15%) to 12 (25%), which agrees well with our values of 8.6–9.5 for this soil

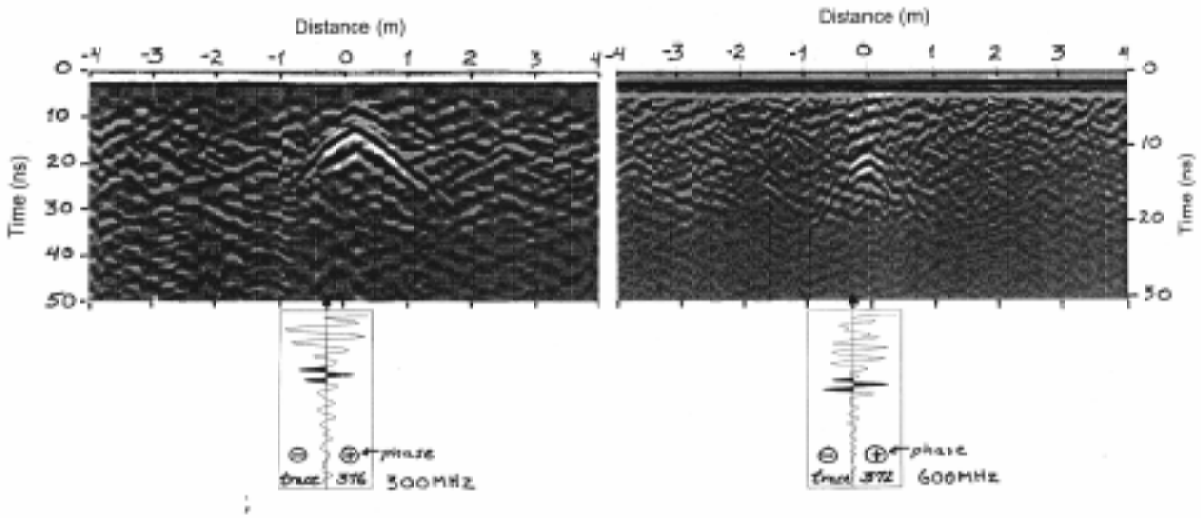

Figure 4. 300- (left) and 600- (right) MHz diffraction profiles and waveform responses to a metal disk buried 58 cm deep. The amplitude of the 600-MHz diffraction fades rapidly as distance increases from the target. The diffracted wavelets (darkened areas) within the sample traces have a half-cycle polarity sequence that is characteristic of the response of this antenna system's wavelets from a metal target.

column. A time-of-flight analysis, in which we ascribed the appropriate ε' to 10-cm soil increments and then calculated the time delay in each increment, gives an effective ε' value of 9.5 (**Fig. 5**, profile 2).

Soil conductivity, σ, was measured at several sites by the Waterways Experiment Station (Llopis et al., in prep.). Using four-electrode Schlumberger soundings, concurrent with our work, they found the soil resistivity structure to be dominated by a near-surface, 2- to 4-m layer with approximately $0.025 < \sigma < 0.04$ S/m. These values strongly influence radiowave attenuation below about 400 MHz, while the imaginary part of ε^*, ε'', influences attenuation above 400 MHz (discussed later). Although ε'' was not measured, the high amount of gain used for the radar measurements indicates a high attenuation rate for this soil and will be seen to be consistent with the above range of σ.

Grid survey: 300 MHz

The transect lines on the 40-acre site are superimposed on maps of target and ordnance distribution in **Figure 3**. The lines surveyed are designated as transects A, B, C, etc. and were 1300 ft (396 m) long. The class of target (ordnance or non-ordnance) is indicated on the map. Additional information regarding exact location and type of target, target depth, and approximate orientation are available. All ordnance are metal.

We show a typical 300-MHz profile segment before and after horizontal background removal filtering in **Figure 6**. Intensity is linearly proportional to signal amplitude in the profile. The time range of 50 ns, beyond which noise became severe, corresponds to about 2.3 m of penetration for ε' = 10.4, the average value obtained at JPG (discussed later). The direct coupling between antennas occupies about 8 ns of the record and masks part of the responses to some of the targets. The noise bands between about 30 and 40 ns are probably caused by radiation leakage onto the cables that reflected back to the receiver and internal system mismatch reflections caused by either the high value of ε' at the surface or poor system design. In both cases, erratic ground contact, caused by uneven topography and jerks in the towing, caused the amplitude of these bands to vary and pre-

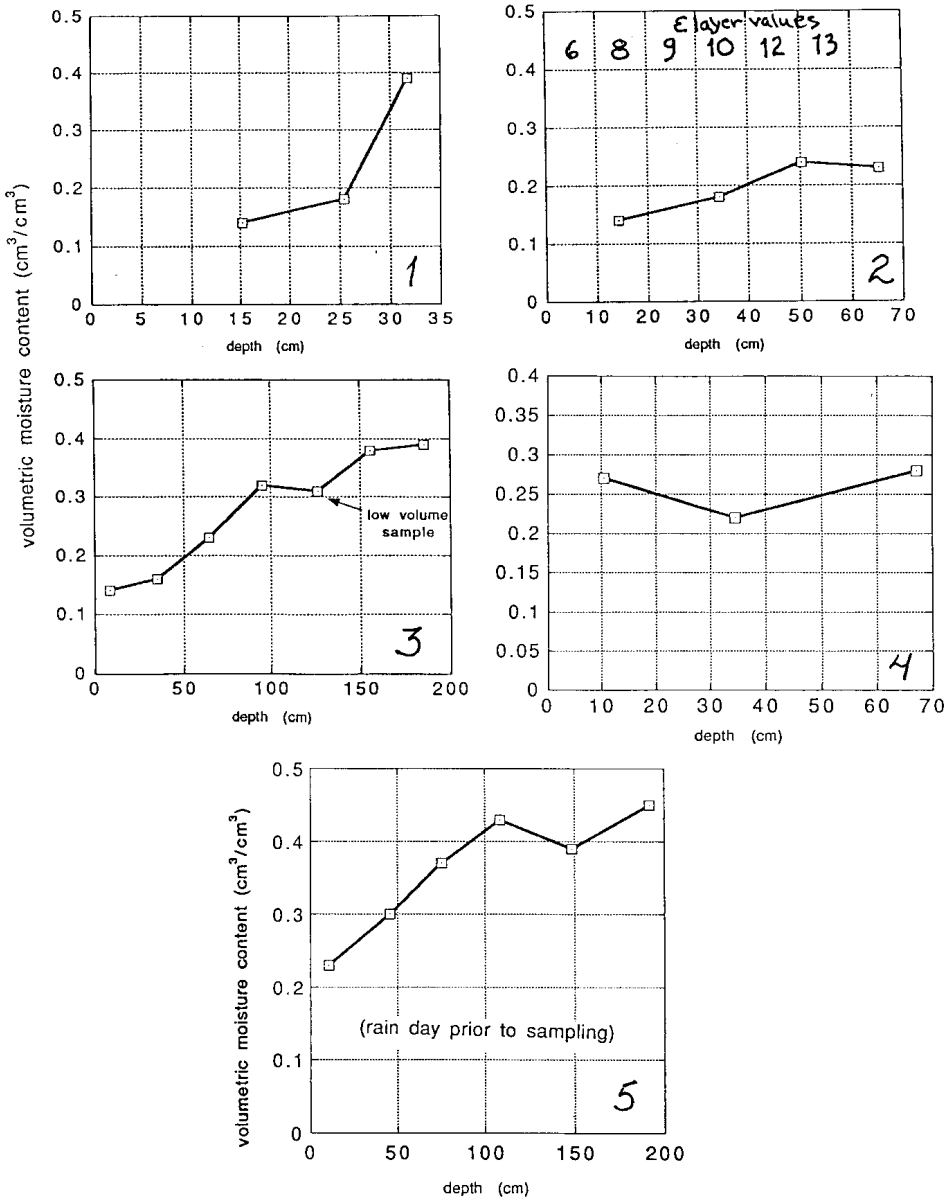

Figure 5. Soil moisture profiles at five locations. Profile #2 is for the soil core extracted to emplace the 58-cm-deep buried target. We show laboratory calibration values (after Topp et al., 1980) of ε' for each 10-cm increment for this profile. Using these values, we then compute an average ε' = 9.5 by calculating the overall propagation time in the soil from the theoretical delays in each of these increments.

cluded the efficacy of horizontal filtering. No distinct and extended horizons indicative of soil stratification or a bedrock interface appear within the 2–3 m of radar penetration along any of our profiles.

We use arrows to identify several targets of anomalously high amplitude in the unfiltered profile of **Figure 6**. These targets are characterized by both hyperbolic diffractions (between 859 and 865 ft)

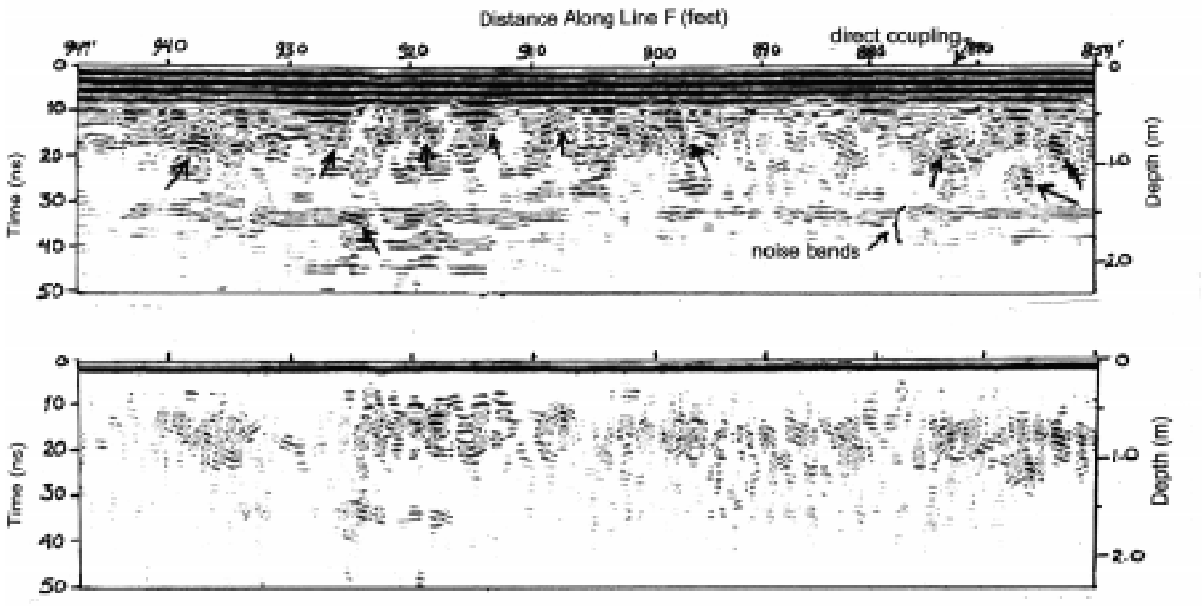

Figure 6. Sample segment of a 300-MHz profile (top) and the result of applying a background removal filter (bottom). The arrows indicate strong targets. The short filter window required to alleviate the erratic character of the background noise decreases the prominence of the target responses.

and short reflection segments. Although the background filtering reduces the noise bands and the direct coupling, it also attenuates many target responses, especially those characterized by short reflection segments such as occur near 926, 915, and 900 ft. The use of more traces (i.e., a wider "window") in the background filter would retain these reflection responses but at the expense of less noise reduction.

In general, we detected a total of 30 high amplitude targets along all 14 lines, of which eight responses are shown within segments of these profiles in **Figure 7**. The phase structure of several of the target wavelets (transects C, left; G, left; K, left; and I, left) identifies them as being of higher impedance than the surrounding soil matrix. They are therefore probably metal. Other target wavelets have a phase structure opposite to that of the metal response (transect F, both left and right; transect K, right). We presume these responses to be from the non-ordnance targets. Some targets exhibit waveform resonance, within which the first few half-cycles have the metal response waveform (transect C, right), while other targets exhibit resonances within the direct coupling and cannot be similarly analyzed (transect G, right; transect L, right). These latter resonances occur where targets are extremely close to the surface; i.e., where target multiple reflections occur before soil attenuation dampens them significantly. In all cases, diffraction asymptotes are so highly attenuated as to be either barely visible for small targets (transect G, left), as was seen in the control studies of **Figure 4**, or not visible at all where they should occur at the ends of short reflection segments recorded above more extended targets (transect C, left).

We give probable interpretations to the target responses seen along transect C (left side) and along transect K (left side) in **Figure 8**. The response along transect C is about 7 ft (2.1 m) long, which is close to the length of a heavy bomb (1.6 m). The location of this response (533–572 ft) is marked in

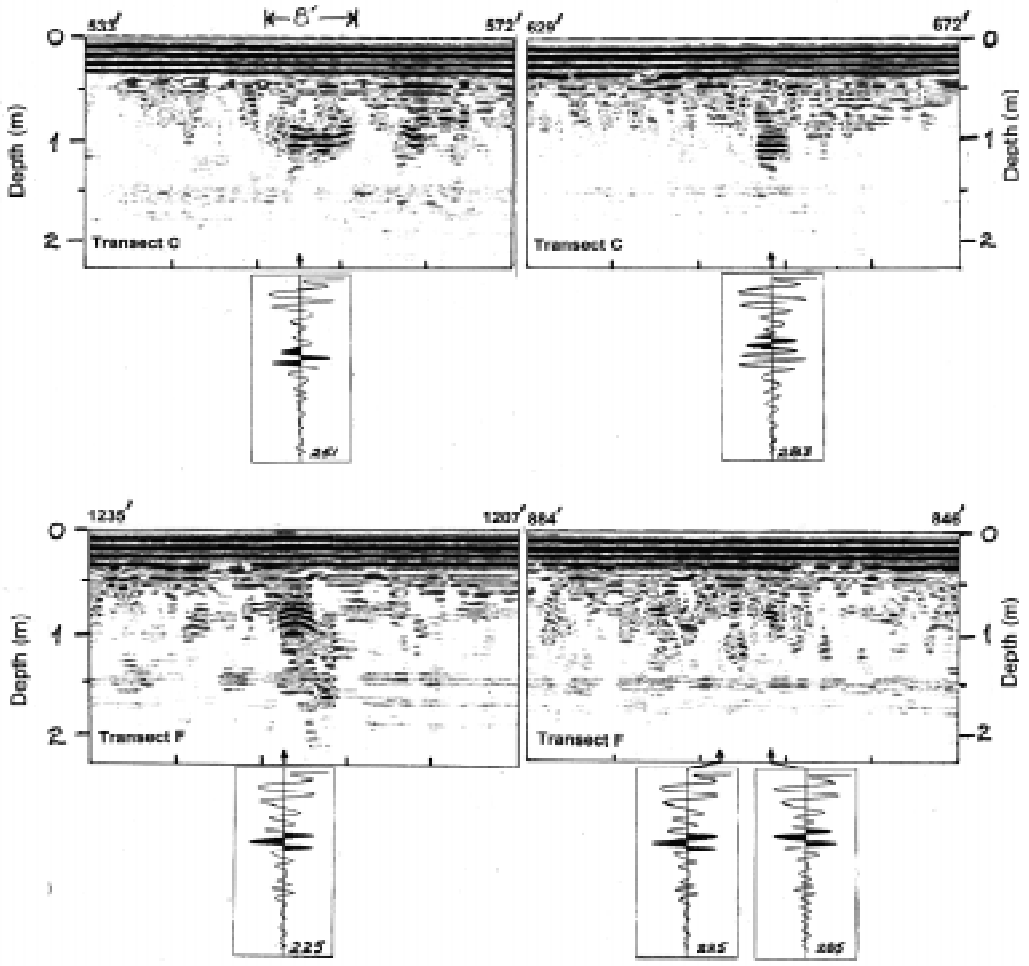

Figure 7. Selected target responses within segments extracted from the 300-MHz profiles and sample traces containing diffracted or reflected wavelets (darkened areas). The distances along each transect are shown at the top of the segments. Each segment is 500 traces long. The depth scale is based on an ε' of 10.4. Many of the wavelets (e.g., transects C, G, K and I) have the same phase as the response to the control target in **Figure 4** and are therefore metal. Responses with the opposite phase (e.g., transects F and K) may be from buried non-ordnance targets. Multiple reflections will also generate the opposite phase, but such phenomena are unlikely to provide separated wavelets at such shallow depths. Consequently the waveforms of some responses show resonance.

Figure 3b as having such ordnance. The more complex response along transect K is about 12 ft (3.7 m) long and occurs in a section marked as having several medium-size mortars and projectiles. The JPG UXO ordnance brochures show many of these projectiles to be about 2 ft (0.6 m) long. We therefore speculate that this transect segment spanned a series of close projectiles.

Grid survey: 600 MHz

We conducted this survey along four of the 14 grid lines. We show profile segments containing the seven strongest target responses (**Fig. 9**) in a nonlinear format because the amplitudes of all the returns are extremely weak, hence the appearance of much more noise (gray speckle patterns) in the profiles than appeared at 300 MHz.

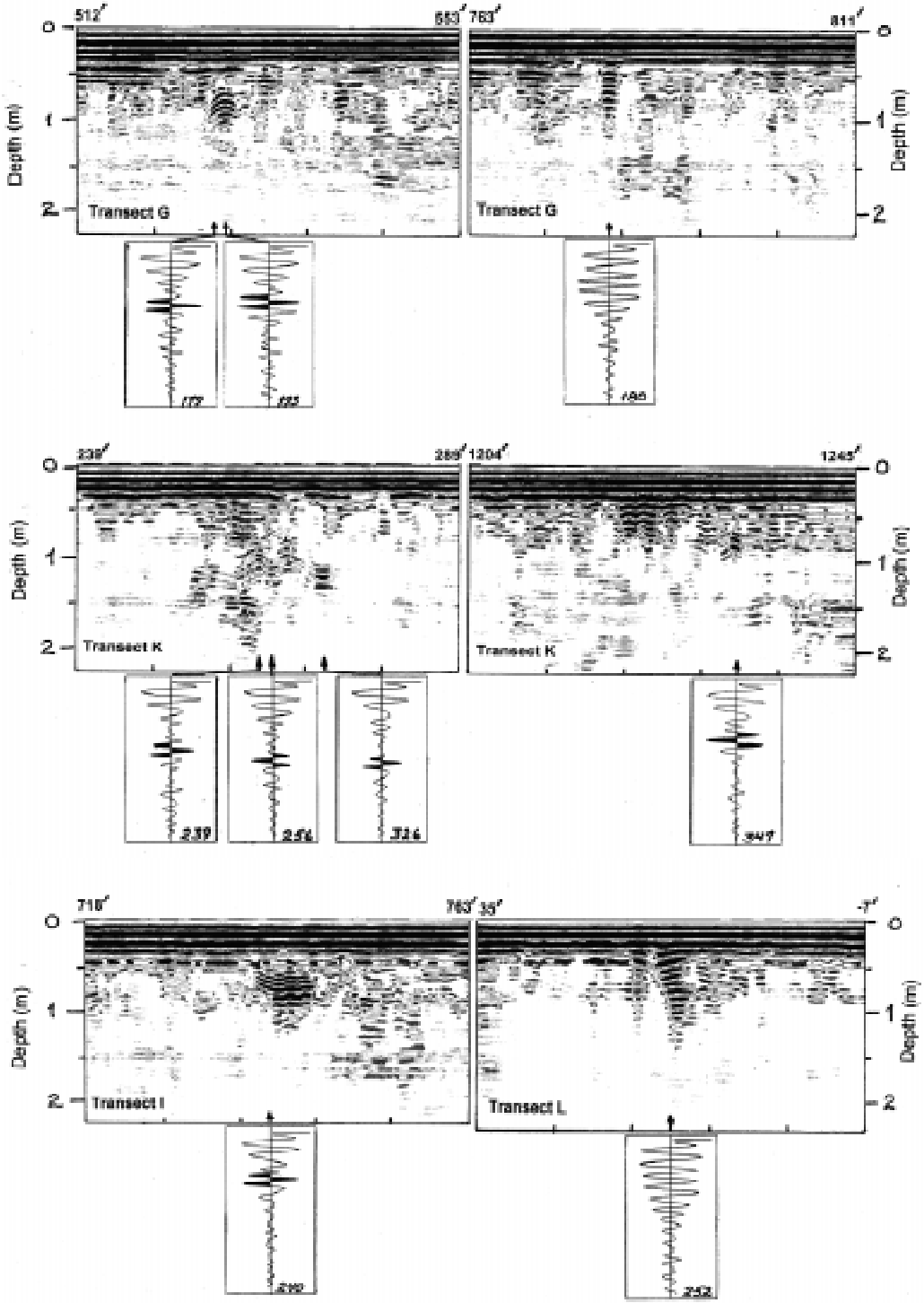

Figure 7 (continued).

Small segments of diffractions are apparent in all the target responses in **Figure 9**; the lack of asymptotes indicates the high signal attenuation. Almost all of the responses have well-defined wavelets that exhibit the proper phase for a high-impedance target. These responses originate from depths less than about 0.5 m and would not have been resolved from the direct coupling of the 300-MHz system. Although the time range is only 30 ns, very few target responses occurred at greater than about 20-ns range. Therefore, the penetration of this frequency in this soil was limited to less than 1 m deep.

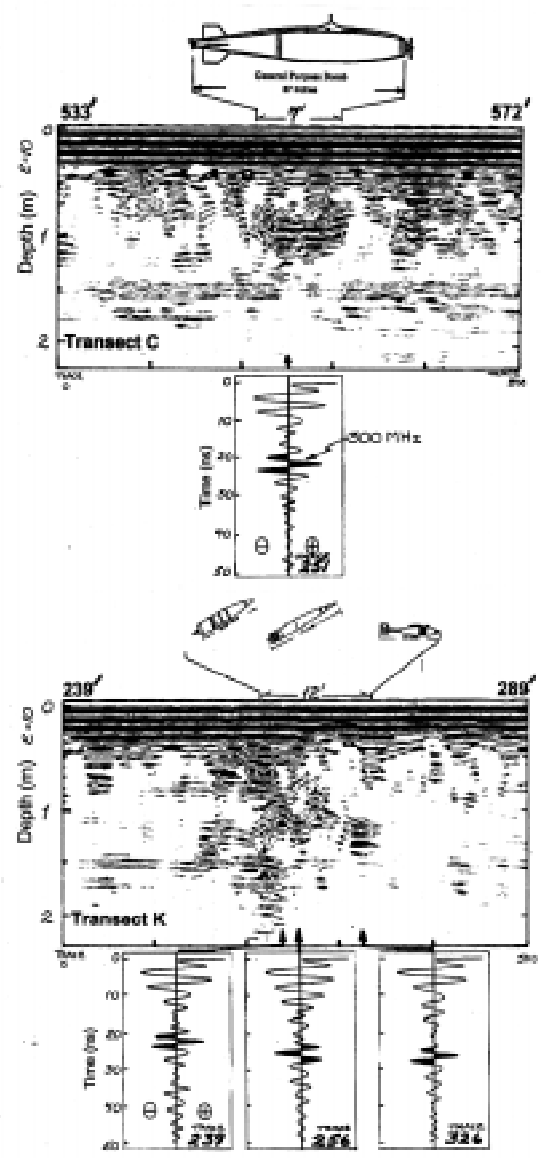

Figure 8. Likely interpretations for two of the responses in **Figure 7**. The transect C target segment is located in **Figure 3b**. The transect K segment is located in an area of concentrated mortars and projectiles (**Fig. 3b**).

Distribution of ε'

We compared the more prominent diffractions seen in both the 300- and 600-MHz surveys with model hyperbolas to produce distributions of ε' and to compute an effective mean permittivity value for the overburden above the targets. Seventy diffractions were identified in the 300-MHz survey and 48 in the 600-MHz survey. We used a statistical approach to average the computational inaccuracies caused by the minor differences in distance scale that resulted from uneven towing speeds. Seventy hyperbolas were clear enough in the 300-MHz profiles to be used and 48 in the 600-MHz profiles. Both distributions (**Fig. 10**) exhibit nearly the same average value and similar standard

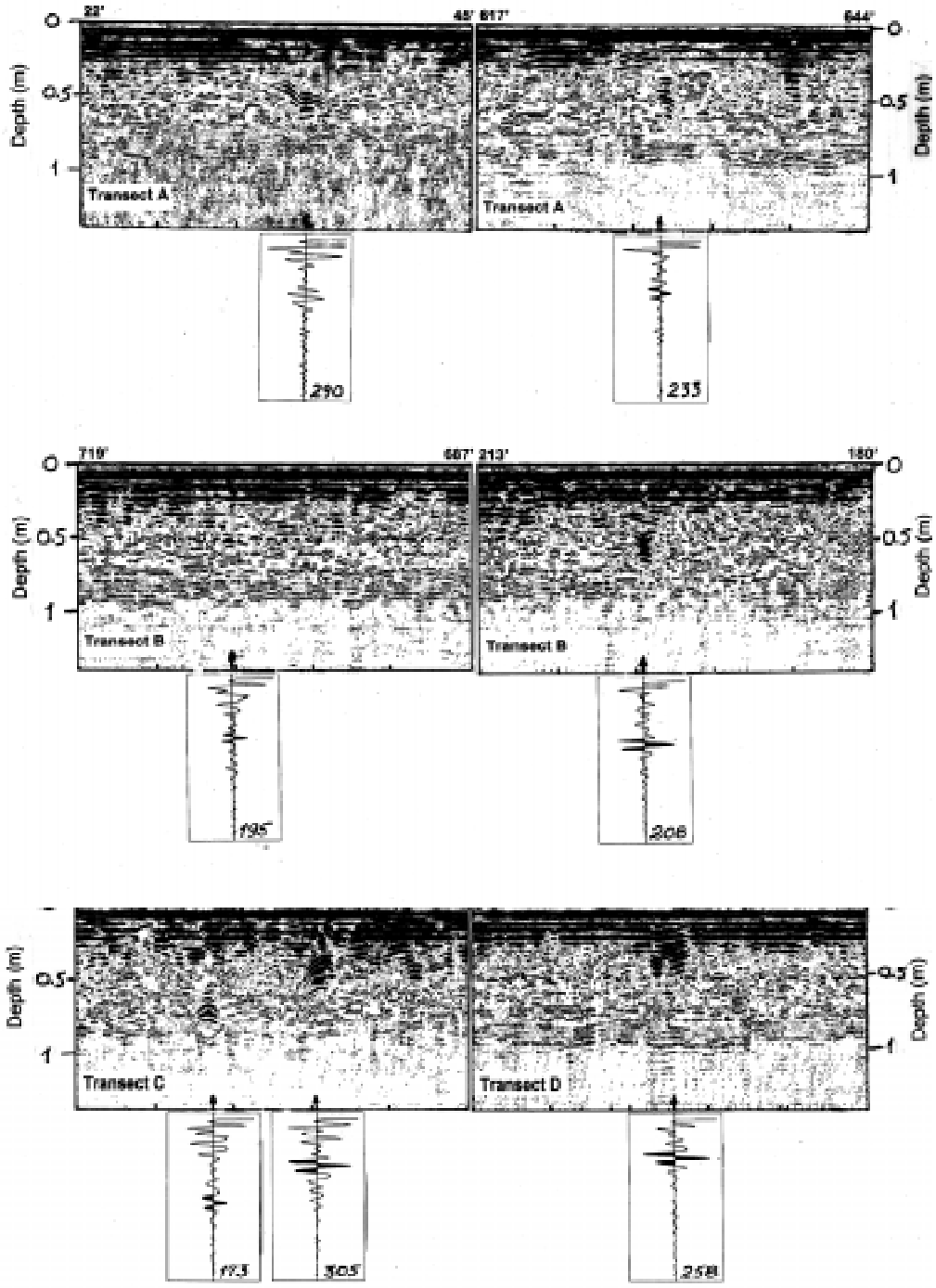

Figure 9. Selected target responses within segments extracted from the 600-MHz profiles and sample traces containing wavelets. The penetration of this frequency is about 1 m.

deviations (s.d.), although their distributions are slightly different. The 300-MHz distribution is more bimodal, which may reflect different orientations of deeper targets; extended targets whose axial direction crosses that of the transect produce hyperbolic reflections rather than diffractions, with values of ε' reduced by the sine of the intersection angle (Jezek et al., 1979). The 600-MHz distribution may reflect less target orientation because it was limited to only lines A–D and to shallower depths.

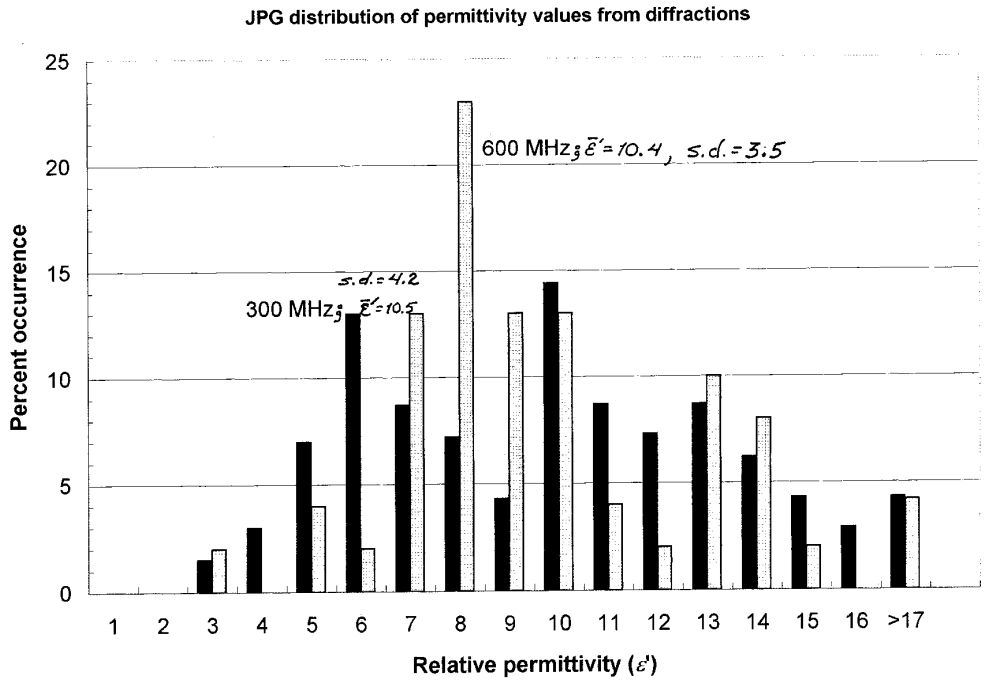

Figure 10. Distribution of ε' at both 300 (black) and 600 MHz (grey).

THEORETICAL DISCUSSION

The average values of ε', the range of σ, the fact that ε' may be slightly less at 600 MHz than at 300, and the high radar gain and faded diffraction asymptotes, both of which indicate high attenuation rates, allow us to estimate the soil dielectric properties at JPG (**Fig. 11a**) and theorize their effect upon antenna beamwidth and waveform. We assume f_{rel} is about 3 GHz (Hoekstra and Delaney, 1974); if it was any lower, then ε' at 600 MHz would be distinctly lower than it is at 300 MHz. We chose a value of 3 for ε_{oo}, which is characteristic of dry soils and applies to frequency values where water is non-dispersive. The JPG values of σ strongly influence β below about 400 MHz, while ε_{rel} is the dominant factor above about 400 MHz (**Fig. 11b**). Unfrozen mineralogic clays can exhibit even stronger absorption and may preclude any radar penetration at our frequency range and above (Hoekstra and Doyle, 1971).

We computed the effects of the soil properties upon the round-trip propagation of both a model of our 300-MHz wavelet and an ideal monocycle type waveform (**Fig. 12**). A monocycle is the shortest possible pulse an antenna can radiate and may be nearly achieved with unshielded antennas. It therefore has a wider bandwidth than our system model and would provide the highest possible target resolution. Both wavelets begin propagation with a local frequency of 400 MHz (**Fig. 12a**), which is that of our antenna model 5103 when used on low-permittivity material (e.g., $\varepsilon' = 4$). Both wavelets then experience strong attenuation caused by conductivity alone (**Fig. 12b**) but maintain their original form in this case and show no shift in local frequency. However, **Figures 12 c–d** show that shifts in local frequency will occur when the dielectric relaxation is considered. Despite the shift, the wavelet form is changed little.

The value of ε' also determines the antenna directivity (Arcone, 1995). Horizontal dipoles on the ground surface show a greater concentration of energy within the subsurface vertical plane that includes the antenna axis than in the plane perpendicular to the axis (**Fig. 13**). As ε' increases, the radiation will become more confined within the plane containing the antenna axis. This means that

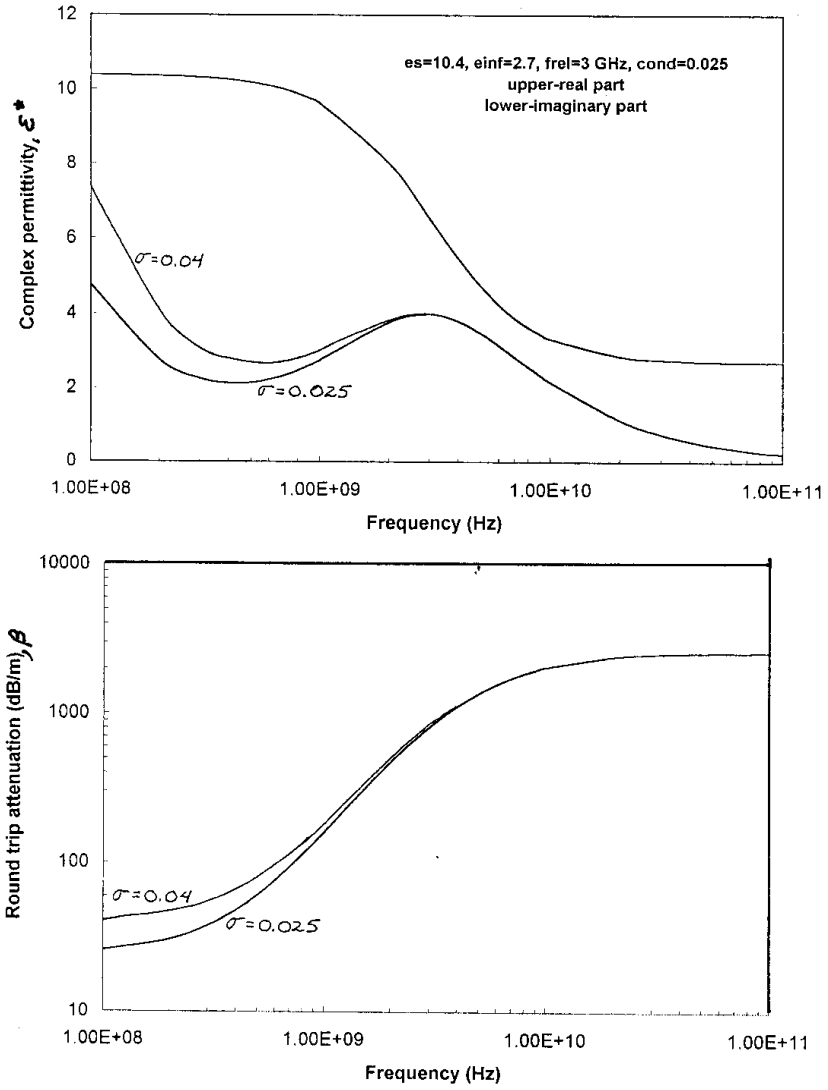

Figure 11. Dielectric permittivity curves (top) and attenuation rates (bottom) for the average ε', range of σ, and probable values of f_{rel} and ε_{oo} at JPG. A dielectric relaxation at about 3 GHz strongly increases β above about 300 MHz, yet wave velocity (determined by the real part of ε_s*) remains constant to about 600 MHz.

our profiles were mainly sensitive to the ground directly beneath the transects. The greater width of the pattern perpendicular to the axis (and along our transects) shows that the rapid fading we observed within diffraction asymptotes was due to soil attenuation and not to radiation directivity.

As an entrance into the modeling, we express the **E** field radiated by a current distribution **J** over the surface of an object as

$$\mathbf{E} = i\omega\mu \iint_S dS' \, \mathbf{G}(r, r') \cdot \mathbf{J}(r') \tag{7}$$

where μ is the medium permeability and S is the surface of the object over which the currents flow.

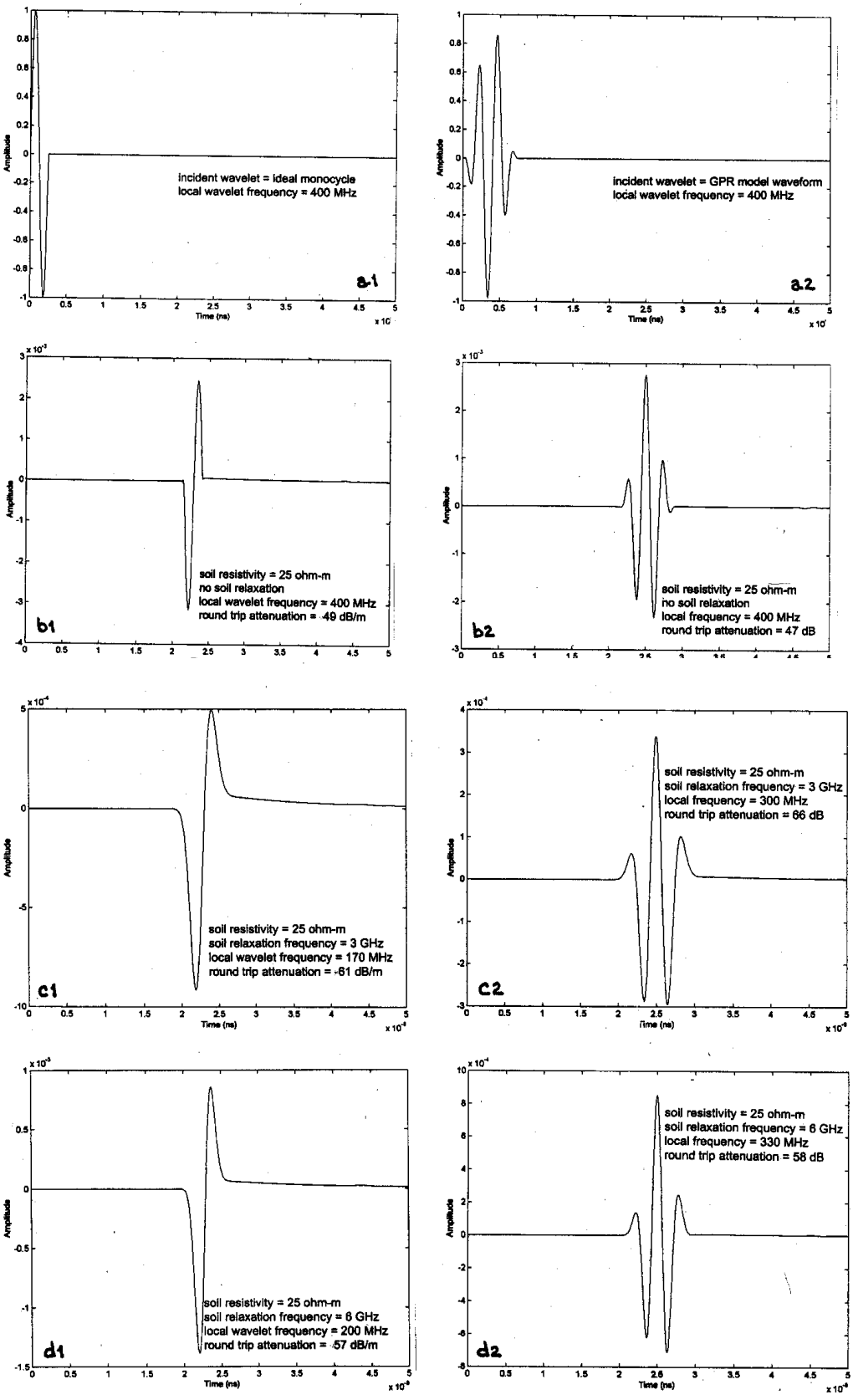

Figure 12. Model 400-MHz wavelets before and after round-trip propagation within 1 m of ground characterized by the soil parameters measured. The wavelets reflect from an interface for which R = -1 (**eq. 6**), which only reverses the phase of the wavelets so that all wavelet distortion and attenuation are due to propagation. The distortion is small in all cases for our system model (**Fig. 12b2, 12c2, 12d2**) and the attenuation is comparable to the gain we used during recording to bring reflections to the level of the direct coupling. The shift in local frequency for the ideal wavelet (**Fig. 12c1, 12d1**) is severe enough to preclude its detection by a receiver antenna identical to the transmitter antenna. In contrast, the local frequency of our system model is lowered to only 300 MHz by the 3-GHz relaxation frequency (**Fig. 12c2**). A value of 6 GHz has less effect (**Fig. 12d2**).

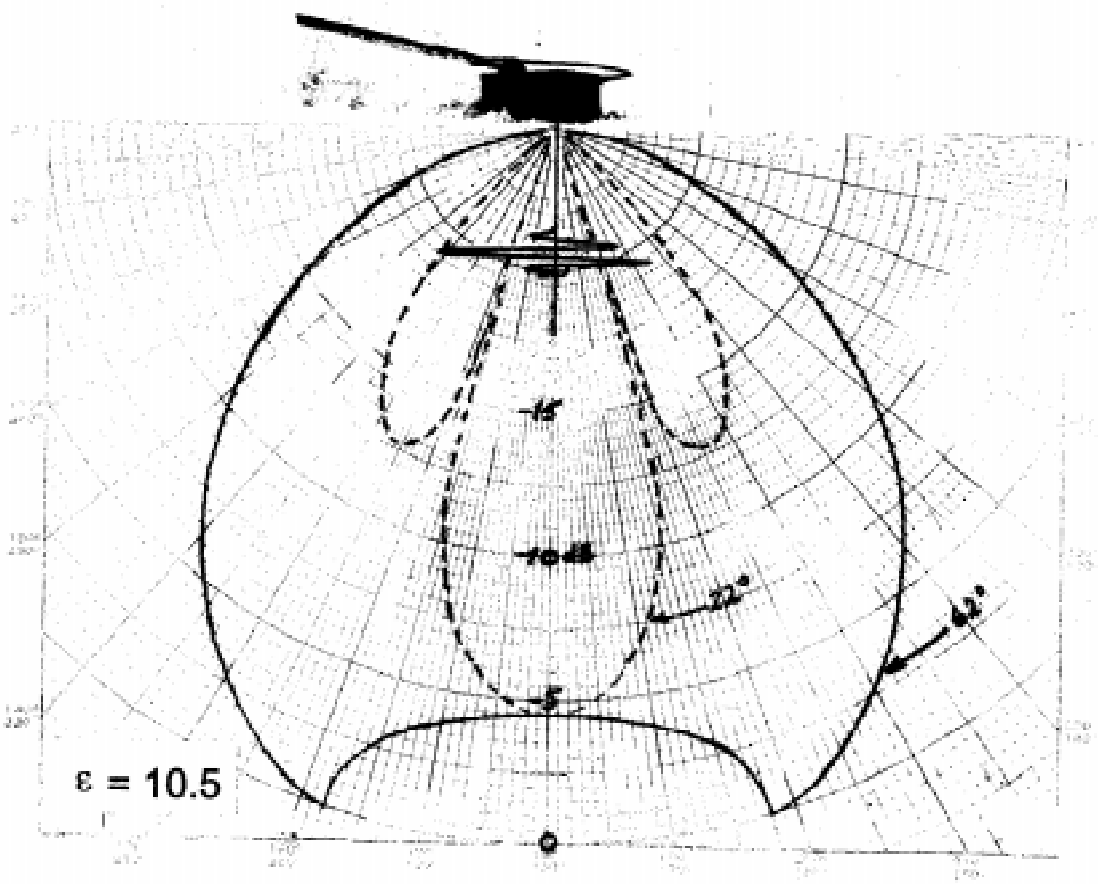

Figure 13. Radiation beamwidths for a model of our antennas and the average ε' = 10.4 found at JPG. The solid curve is the beam pattern within the plane of the transect and is perpendicular to the direction of antenna polarization. The dotted curve is the beam pattern in the plane of the antenna polarization, which is perpendicular to the transect direction. Individual pattern 3-dB beamwidths are indicated at the point of the arrows. The more narrow beamwidth is in the plane perpendicular to the transects, which shows why the radar profiles are sensitive mainly to the ground beneath the transect. A typical radiated wavelet is shown beneath a photo of the antenna transducer. The curves assume that the transmitter and receiver antennas are coincident. They are actually spaced about 15 cm apart in the 300-MHz unit and slightly less in the 600-MHz unit.

G is the diadic Green's function, containing the scalar Green's function *g*.

$$\mathbf{G} = \left[\mathbf{I} + \frac{1}{k^2}\nabla\nabla\right] g$$

$$g = \frac{e^{ikR}}{4\pi R}, \qquad R = |\, r - r' \,| \tag{8}$$

The point **r** is an observation point, while **r′** is a source point on the object. For a more complete explanation of these quantities and their sense, the reader is referred to an appropriate fundamental

electromagnetics treatment (e.g., Kong, 1990).

We may use the expressions (7) - (8) for a variety of purposes here: to calculate the incident field from an antenna with arbitrary dictated current distribution; and for the reradiated (scattered) field from the target, as perceived by our sensor, once we have used other means to determine the currents induced on the target. Substituting (8) into (7) and carrying through various manipulations produces the ultimate expressions for the electric field scattered by **J**. The concomitant H field is most easily obtained by applying Maxwell's equations to (7) first, then performing the manipulations.

$$\mathbf{E}^{scat} = i\omega\mu \iint_S dS' \frac{e^{ikR}}{4\pi R k^2}\left\{(1+A_1)\mathbf{J} + A_2\left(\hat{\mathbf{R}}\cdot\mathbf{J}\right)\hat{\mathbf{R}}\right\}$$

$$A_1 = \frac{1}{R}\left(ik - 1/R\right) \qquad A_2 = \left(ik - 1/R\right)^2 + 1/R^2 - A_1 \tag{9}$$

$$\mathbf{H}^{scat} = \iint_S dS' \frac{e^{ikR}}{4\pi R k^2}\left(ik - 1/R\right)\left(\hat{\mathbf{R}}\times\mathbf{J}\right)$$

In the modeling done here, currents on the targets were obtained in two ways: from detailed finite element modeling (Haider et al., in prep.) and from an analytical model developed by J.R. Wait (1955). We will discuss the latter here.

To use Wait's expressions we assume 1) that the scattering behavior of UXO-like object can be approximated by a finite-length circular cylinder, and 2) the scattering behavior of such a finite cylinder may be approximated from the scattered fields produced by currents on segments of an otherwise similar infinite cylinder. We take the Z axis to be aligned with the longitudinal target (cylinder) axis, while the vertical coordinate pointing up towards the ground surface is X. Incidence is in the (X,Z) plane, and the incident E field is polarized in that plane (i.e. $E_y^{inc} = 0$, $H_z^{inc} = 0$).

To obtain the currents generated on the target surface by a plane wave impinging at an angle θ_i relative to the negative Z axis, we evaluate the total tangential H field on the cylinder surface, which is the sum of the incident and scattered H fields.

$$H_\phi^{inc} = \sum_{n=-\infty}^{\infty} \frac{-ik}{\mu\omega} i^n J_n'(v) F_n(z,\phi)$$

$$H_\phi^{scat} = \sum_{n=-\infty}^{\infty} \frac{-ika_n^s}{\mu\omega\sin(\theta_i)} H_n^{(2)\prime}(v) F_n(z,\phi) \tag{10}$$

where J_n and $H_n^{(2)}$ are Bessel and Hankel functions,

$$v = k\sin(\theta_i)a \qquad F_n = \exp\left\{-i\left(n\phi + kz\cos(\theta)\right)\right\} \tag{11}$$

and a is the cylinder radius. (In all expressions from Wait, we retain his assumption of $e^{i\omega t}$ time dependence but assume the negative time exponent in all other expressions.) The coefficients a_n^s are evaluated for a perfectly conducting target as

$$a_n^s = -\frac{J_n(v)}{H_n^{(2)}(v)} i^n \sin(\theta_i) \tag{12}$$

per unit incident field. To simplify calculations in the petit examples here, we do not use (7) to obtain the incident field from our antenna but assume that it radiates an approximately spherical wave

$$E^{inc} \sim \frac{e^{ikR_a}}{R_a} \cos^2\left\{\frac{\pi}{2}\left(\theta_a \big/ \theta_b\right)\right\} \tag{13}$$

where R_a is the distance from the antenna to a point on the target, θ_a is the angle to that point from the antenna look direction (vertically downward below its location), and θ_b is a parameter expressing the subsurface beam width, taken here to be 65°. For θ_a greater than θ_b we take the beam to be zero. Additionally, in using (13) for this (or any) beam instead of a plane wave, we are assuming that the incident field is *locally plane* over each small length segment of the cylinder. Beyond that, to perform the calculations we must adjust the z-dependent phase factor in F_n in accordance with the actual phase variation of E^{inc} along Z, not as per the planar variation assumed in (11). We do this for each segment of the cylinder along its length, determining the local incidence geometry, induced current, and scattered field, and summing the latter from all length segments.

Using these expressions and an analytical expression for the transform of the transmitted wavelet, we solve the entire system for each frequency, determine the scattered fields from (1), and invert the result for a time domain rendering. Figures 14 and 15 show example results for a soil assumed to have relative dielectric constant of 10 + *i*. The wavelet center frequency is 300 MHz, and cylinder dimensions are 0.26 m diameter and either 2.2 m in length (the "1 × 5" cylinder, taken to approximate a general purpose bomb, as found at Jefferson Proving Ground), or 0.26 m in length (the "1 × 1" cylinder). Burial depth (distance below the antenna's survey transect) is 1 m. The synthesized radar returns in the plots below have been scaled, obscuring the fact that the response from the smaller target is approximately 4 dB below that of the larger. We note that the long cylinder produces a fairly level response. Its amplitude fades near the ends of the target with much change in delay (t). (Amplification shows some hyperbolic fall off in the pattern beyond the cylinder ends, but this is very much a secondary feature in this picture.) For the very short cylinder, we do not expect great accuracy in results based on currents from the solution for a segment of an infinite cylinder. Nevertheless, detailed numerical treatments have suggested that even for such cases the results are reasonable for normal (transverse) incidence positions, and they are still in the ballpark at angles around that. Thus the model suffices to make our point here. We note the curved trajectory of the wavelet positions in the traces in Figure 15, as indicated by the curve drawn above the reflections.

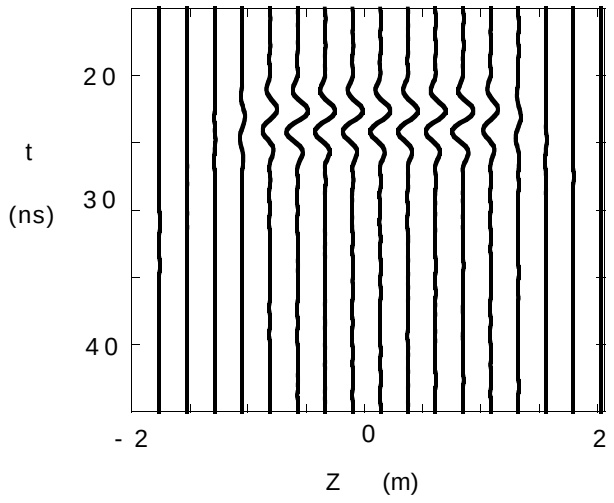

Figure 14. Returns for a 1 × 5 cylinder at 25-cm intervals in Z.

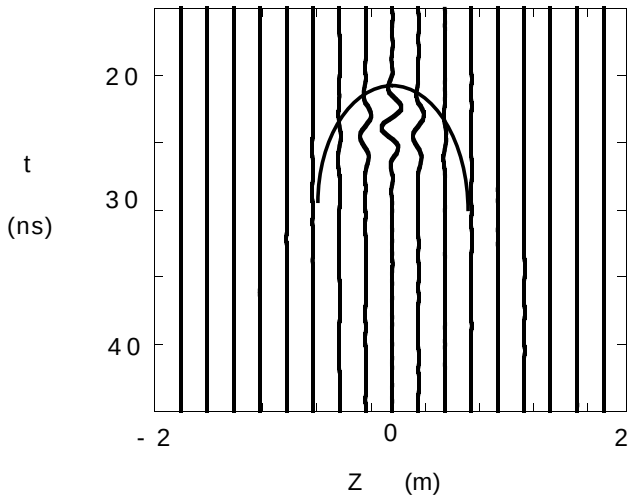

Figure 15. Returns for a 1×1 cylinder at 25-cm intervals in Z.

As it survives this and other more detailed tests of reasonableness, we use this simple model to examine likely effects of depth, frequency-dependent soil character, target size and aspect ratio, and disposition. This simple model is being combined with a suite of vehicles, from analytical to detailed numerical, to investigate environmental influences, evaluate sensing strategies, and identify innovative signature approaches.

CONCLUSIONS AND RECOMMENDATIONS

1. Soil attenuation at JPG was extremely high, as evidenced by the high amount of gain required to display the signals received from within only the first meter of depth. The gain values of 50–65 dB that we applied are consistent with the general values of round-trip attenuation for 1 m of depth predicted by our propagation models. GPR bandwidths should be centered no higher than 600 MHz because the round-trip attenuation per meter of depth above this frequency may exceed the dynamic range of the radar. This fact precludes the use of any microwave system for detection of UXO. These high attenuation rates also greatly reduce off-axis sensitivity to targets so that full-diffraction signatures are rarely seen. We therefore recommend that the antenna towing speeds be kept very slow and data acquistion rates very high to ensure recording of as much of the diffraction responses as possible. We further recommend that an all digital system eventually be developed so that extremely high rates (e.g., 512–1024 traces/s) would further allow noise reduction by trace stacking.

2. The most likely range of soil dielectric constants (5–14) is consistent with the measured moisture contents. The average value of about 10 predicts a narrow beamwidth in the plane parallel with the antenna polarization axis. This means that for normal towing operations, wherein the antennas are polarized perpendicular to the transect direction, the system is sensitive to ground mainly beneath the antennas. We therefore recommend that coverage be increased by using a multi-channel radar system. Such operation is standard with present commercial systems, but its implementation compromises the data acquistion rate. Therefore, this is further reason for development of a real-time digitizing GPR system above 300 MHz that could acquire data at 512–1024 traces/s.

3. Horizontal filtering, normally an effective means of reducing weak internal and external noise (or clutter) that occurs at constant time delay, was only partially successful. We have ascribed this result to the effects of uneven towing speeds and erratic contact between the ground surface and

antenna faces upon antenna leakage. We recommend that a simple antenna platform, consisting of a heavy, high-density polyethylene "boat," be used to contain the antenna. The prow of the boat would help to deflect vegetation, and the weight will improve ground contact. The dielectric permittivity of the material is intermediate between air and ground and may improve the antenna impedance match with the near surface. The use of this platform may make the amplitude of the clutter bands more uniform and subject to better removal with horizontal filters.

4. We recommend that improved jitter control be specified in the design of future transmitters and receivers. Jitter is the slight shift in time that occurs in signal position from trace to trace. Although jitter may only be 1–2 ns, its reduction could significantly reduce noise when the trace length is only 30–50 ns.

5. We recommend that antennas for UXO detection remain on the surface. Airborne profiling, even at minimal heights of a few tens of centimeters, introduces an extra dielectric layer (air) into the propagation medium. In airborne profiling, returns from uneven subsurface interfaces will be strongly refracted along the surface and not be received because the value of $\varepsilon' = 1$ for air contrasts sharply with the ε' of the soil.

6. The wavelet shape transmitted by present, commercially available systems is probably most practical. Our theoretical studies show that shorter pulse length, which may be available with unshielded antennas, may shift too much in local frequency to be detected after propagation.

7. Future surveys should address the problem of total soil saturation. Our surveys were conducted in early fall, by which time these soils are usually below saturation. However, saturation levels are usually reached by late winter and can persist into late spring. Saturated soils have higher values of ε_s* and f_{rel} and may therefore offer less attenuation per meter at 300–600 MHz than would moist soils. However, mechanical operation in mud may be a serous mobility problem.

REFERENCES

Arcone, S. A. (1995). Numerical studies of the radiation patterns of resistively loaded dipoles. *Journal of Applied Geophysics*, **33**, 39-52.

Arcone, S. A., Lawson, D. E., Delaney, A. J., Strasser, J. C. and Strasser, J. D. (1998). Ground-penetrating radar reflection profiling of groundwater and bedrock in an area of discontinuous permafrost. *Geophysics*, in prep.

Brillouin, L. (1960). *Wave propagation and group velocity*. Academic Press: New York.

Clarke, T. S., and Bentley, C. R. (1994). High-resolution radar on Ice Stream B2, Antarctica: Measurements of electromagnetic wave speed in firn and strain history from buried crevasses. *Annals of Glaciology*, **20**, 153-159.

Delaney, A. J. and Arcone, S. A. (1984). Dielectric measurements of frozen silt using time domain reflectometry. *Cold Regions Science and Technology*, **9**, 39–46.

Debye, P. (1929). *Polar Molecules*. Dover Publications: Mineola, New York.

Feynman, R. P., Leighton, R. B. and Sands, M. (1964). *The Feynman Lectures on Physics, Vol. II*.

AddisonWesley: Reading, Massachusetts.

Haider, S. A., O'Neill, K. and Paulsen, K.D. (in prep.) 3-D simulation of subsurface pec sensing for discrimination enhancement using bistatic positional, angular, and polarization diversity. International Geoscience Remote Sensing Symposium 1998, Seattle.

Hoekstra, P. and Delaney, A. J. (1974). Dielectric properties of soils at UHF and microwave frequencies. *Journal of Geophysical Research*, **79**, 1699–1708.

Hoekstra, P. and Doyle, W. T. (1971). Dielectric relaxation of surface adsorbed water. *Journal of Colloid and Interface Science*, **36**, 513–521.

Jezek, K. C., Bentley, C. R., and Clough, J. W. (1979). Electromagnetic sounding of bottom crevasses on the Ross Ice Shelf, Antarctica. *Journal of Glaciology*, **24**, 321-330.

Kong, J.A. (1990) *Electromagnetic Wave Theory,* John Wiley and Sons: New York.

Llopis, J. et al. (in prep). Soil resistivity measurements at JPG.

NAVEOD. (1997). *Unexploded ordnance (UXO): An overview*. Naval Explosive Ordnance Disposal Technology Division, UXO Countermeasures Department, Indian Head, MD.

Nickell, A. K. (1985). *Soil Survey of Jefferson County, Indiana*. U. S. Dept. Agriculture, Soil Conservation Service, 169 pp. with maps.

Parkhomenko, E. I. (1967). *Electrical properties of rocks*. Plenum Press: New York.

Pewe, T. L. (1955). Origin of the upland silt near Fairbanks, Alaska. *Geological Society of America Bulletin*, **67**, 699-724.

Rodbell, D. T., Forman, S. L., Pierson, J. and Lynn, W. C. (1997). Stratigraphy and chronology of Mississippi Valley loess in western Tennessee. *Geological Society of America Bulletin*, **109**, 1134-1148.

Stratton, J. (1941). *Electromagnetic Theory*. McGraw-Hill: New York.

Tice, A. R., Oliphant, J. L., Nakano, Y. and Jenkins, T. F. (1982). Relationship between the ice and unfrozen water phases in frozen soil as determined by pulsed nuclear magnetic resonance and physical desorption data. *CRREL Report 82-15*, U. S. Army Cold Regions Research and Engineering Laboratory, Hanover, NH, 8 pp.

Topp, G. C., Davis, J. L. and Annan, A. P. (1980). Electromagnetic determination of soil water content: Measurements in coaxial transmission lines. *Water Resources Research*, **16**, 574–582.

Wait, J.R. (1955) Scattering of a plane wave from a circular dielectric cylinder at oblique incidence. *Canadian Journal of Physics*, **33,** 189–195.

Wait, J. R. (1970) *Electromagnetic waves in stratified media, 2nd Ed*. Pergamon Press: New York**.**